Imaging of Heterogeneous Materials with a Turbo Spin Echo Single-Point Imaging Technique

Steven D. Beyea, Bruce J. Balcom,[1] Igor V. Mastikhin, Theodore W. Bremner,*
Robin L. Armstrong, and Patrick E. Grattan-Bellew†

*MRI Centre, Department of Physics, and *Department of Civil Engineering, University of New Brunswick, P.O. Box 4400, Fredericton New Brunswick, Canada E3B 5A3; and †Institute for Research in Construction, National Research Council of Canada, Ottawa Ontario, Canada K1A 0R6*

A magnetic resonance imaging method is presented for imaging of heterogeneous broad linewidth materials. This method allows for distortionless relaxation weighted imaging by obtaining multiple phase encoded k-space data points with each RF excitation pulse train. The use of this method, turbo spin echo single-point imaging-(turboSPI), leads to decreased imaging times compared to traditional constant-time imaging techniques, as well as the ability to introduce spin–spin relaxation contrast through the use of longer effective echo times. Imaging times in turboSPI are further decreased through the use of low flip angle steady-state excitation. Two-dimensional images of paramagnetic doped agarose phantoms were obtained, demonstrating the contrast and resolution characteristics of the sequence, and a method for both amplitude and phase deconvolution was demonstrated for use in high-resolution turboSPI imaging. Three-dimensional images of a partially water-saturated porous volcanic aggregate ($T_{2L} \approx 200$ ms, $\Delta\nu_{1/2} \approx 2500$ Hz) contained in a hardened white Portland cement matrix ($T_{2L} \approx 0.5$ ms, $\Delta\nu_{1/2} \approx 2500$ Hz) and a water-saturated quartz sand ($T_2 \approx 300$ ms, $T_2^* \approx 800$ μs) are shown. © 2000 Academic Press

Key Words: MRI; single-point; SPI; turboSPI; concrete; porous materials.

INTRODUCTION

The use of nuclear magnetic resonance (NMR) for studying and characterizing bulk properties of porous media has been demonstrated by many authors (*1–5*). The extension to spatially resolved methods using MRI has demonstrated the difficulties involved in obtaining good signal-to-noise (S/N) high-resolution images of highly heterogeneous media (*1, 6–10*). Porous materials frequently possess low fluid contents and short spin–spin relaxation times, both of which contribute to poor-quality NMR images (*6*). In addition, the difference in magnetic susceptibility between the pore fluid and the solid matrix leads to a large distribution of magnetic fields within the porous materials and correspondingly broad NMR linewidths (*2*). Images of such porous media have been obtained using spin-echo (SE) (*8, 9*), gradient echo (*9*), and π-echo-planar (π-EPI) (*10, 11*) imaging methods. Images acquired using all of these methods exhibit, to varying degrees, distortion and resolution loss in the frequency encode direction.

Image distortion and resolution loss due to susceptibility heterogeneities can often be overcome through the use of very strong frequency encoding gradients (*8–12*). Acquiring image data in the presence of strong gradients, however, comes at the expense of increased acquisition bandwidth, leading to a proportional decrease in S/N. The optimum acquisition bandwidth when frequency encoding, in the absence of diffusion, is $N(\Delta\nu_{1/2})$, where $\Delta\nu_{1/2}$ is the inhomogeneously broadened linewidth. This is the minimum bandwidth necessary to have the frequency width of a pixel equal to that of the natural linewidth. Sarkar *et al.* (*9*) discuss the requirement of doing as many as 50 signal averages in order to accurately interpret two-dimensional SE images of porous sintered glass disks. This problem is compounded when imaging in the presence of molecular diffusion. It is well known that diffusion effects can be minimized through the use of stronger gradients applied for shorter periods of time (*13, 14*). This requires a frequency encoding acquisition bandwidth greater than the optimal value required to resolve the image, leading to a further decrease in S/N.

Pure phase encoding techniques are often useful for imaging highly heterogeneous samples, due to the fact that images acquired with this technique do not contain artifacts due to chemical shift, susceptibility variations, or imperfect B_0 shimming (*13–20*). However, while pure phase encode methods are excellent at obtaining high-resolution "artifact-free" images, it is generally accepted that these methods are slow (*21*), as they require N^2 excitations for a 2D image of N^2 pixels. This is typically true, however, only because traditional spin-warp (frequency-phase) (*22*) methods are routinely used on systems with intrinsically large NMR signals and long signal lifetimes, and the subsequent images are usually acquired with little or no signal averaging (*14, 15*). When significant signal averaging is necessary, such as in high-resolution imaging and imaging of heterogeneous materials (e.g., porous media), it can be shown that pure phase encoding is equally time efficient.

[1] To whom correspondence should be addressed.

The optimal acquisition bandwidth with pure phase encoding is simply $\Delta\nu_{1/2}$, due to the fact that the encoded signal is not acquired in the presence of a gradient. A 2D frequency-phase image, with an acquisition bandwidth N times larger, suffers from a S/N which is $N^{1/2}$ times smaller per signal average. Therefore, although 2D pure phase encoding requires N times more phase encode steps than a 2D frequency-phase image, frequency encoding requires N signal averages to obtain an image with the same S/N ratio as a single-scan purely phase encoded image (14). Thus, in situations where N frequency encoded signal averages are necessary to produce an image with no blurring or susceptibility artifacts, we see that pure phase encoding has equivalent time efficiency (14, 15). We note as well that phase encoding gradient strength can be increased both to increase resolution and to minimize diffusional losses, without a subsequent increase in acquisition bandwidth.

We have frequently encountered samples where we would require very large gradients to obtain images free of susceptibility-induced artifacts when frequency encoding, while needing to avoid the subsequent increase in acquisition bandwidth in order to maintain adequate sensitivity. In this paper we present a pure phase encode method which avoids susceptibility artifacts while having a high S/N per signal average. The proposed method allows the introduction of relaxation contrast with long effective echo times, while keeping the time between refocusing pulses short and decreased imaging times through the acquisition of multiple phase encoded k-space data points per RF excitation, obtained in a longitudinal steady state.

PREVIOUS METHODS

Multiple Phase Encoded Spin Echo Methods

Several methods have been proposed, using pure phase encoding techniques, to avoid image artifacts associated with magnetic field inhomogeneity and chemical shift, while increasing time efficiency through the acquisition of multiple k-space points per RF excitation (23–25). Sharp et al. (23) attempted to avoid distortions with heterogeneous materials through of the use of a half-Fourier method which samples a single point at the maxima of a spin echo train. The k-space coordinate is stepped between the acquisition of each data point through the use of an EPI-type blipped gradient. The refocused gradient method of Miller and Garroway (24) also eliminates the effects of chemical shift and susceptibility, but requires that data be obtained in the presence of the gradient, thereby increasing the acquisition bandwidth. Both of these methods are susceptible to artifacts caused by the encoding and acquisition of stimulated echoes.

McIntyre et al. (25) have proposed a method, once more sampling the echo maxima of a spin echo train, with RARE (rapid acquisition with relaxation enhancement) (26, 27) phase encoding between successive echoes. The use of RARE-type gradients refocuses all phases accumulated during the encoding period prior to the application of the next refocusing pulse. In this way, all echoes (spin and stimulated) have the same encoding. This sequence, called SPARE (single point acquisition with relaxation enhancement) (25), is free of artifacts due to stimulated echoes and is relatively insensitive to B_1 inhomogeneity. The SPARE method as described by McIntyre et al. acquires 128 data points per RF excitation and is therefore applicable only to long T_2 materials. This method also uses slice selective RF pulses and is intended for distortion free imaging in the presence of a poorly shimmed inhomogeneous $\mathbf{B}_0$ field over the volume of the sample. For materials such as porous rocks, however, this method is not viable, both because rapid T_2^* relaxation during the shaped RF pulse negate the use of slice selection and because of the decrease in sensitivity due to severe T_2 weighting at the k-space center. The SPARE technique is, however, quite robust and immune to image distortion and artifacts, with increased time efficiency over traditional single-point methodologies.

TURBO SPIN ECHO SINGLE-POINT IMAGING (turboSPI)

Basic Sequence

We propose a new single-point imaging technique, based on the RARE (26, 27) and turboFLASH (28, 29) imaging methods, which is capable of obtaining high resolution T_2-weighted images of heterogeneous materials with decreased imaging times compared to standard pure phase encode methods. This method retains the various benefits of the sequences discussed above for imaging of heterogeneous materials with large natural linewidths. We believe this sequence to be optimal for T_2-weighted imaging of porous materials with broad NMR linewidths with required resolution in the range of several hundred micrometers.

The turboSPI sequence uses hard (broadband) excitation and refocusing pulses combined with RARE-type bipolar phase encoding gradients, as shown in Fig. 1 for an experiment with an echo train length (ETL) of eight. All refocusing pulses are full 180° RF pulses, so as to obtain the maximum possible refocused magnetization. The gradient set used in these experiments had switching times of approximately 100 μs on all axes, which leads to a minimum phase encoding time (t_p) of approximately 200 μs when implemented on our system. We wish to maintain short encoding times so as to minimize the time for diffusion through field gradients and to minimize the τ time ($\tau_{min} \approx 2t_p$), both of which limit diffusion-based signal loss. While this sequence also utilizes very small audio filter bandwidths to obtain high S/N per average, we note, however, that the ringdown time of the bandpass filter (in our case a four-pole Butterworth), sometimes forced us to use filter bandwidths slightly larger than the optimum value.
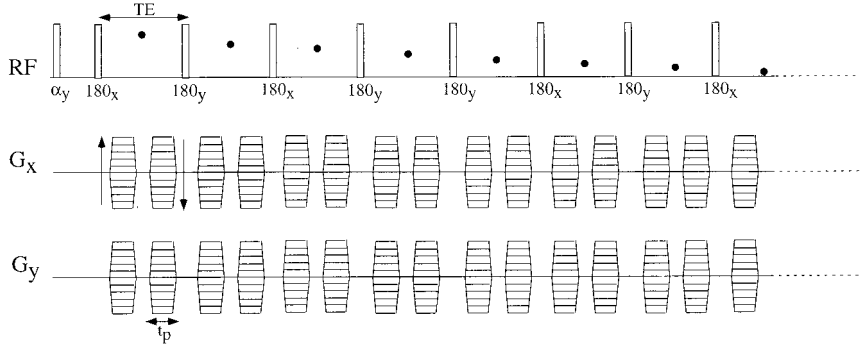
FIG. 1. The two-dimensional turboSPI pulse sequence. Pure phase encoding is used on all axes, with zero net gradient area between refocusing pulses, so as to avoid stimulated echo artifacts. The sequence uses Ernst angle excitations, and an XY-8 or XY-16 refocusing train of 180° pulses, where α is the RF excitation flip angle, and t_p is the phase encoding time. The repetition time is the time between the end of the echo train and the next excitation pulse and is generally less than $5*T_1$. Echo trains of 8 to 16 echoes are typically used, and the various k-space data points are reordered during image processing.

Dynamic Equilibrium turboSPI

A common method of decreasing imaging times is to acquire the data in a longitudinal steady state using Ernst angle excitations to avoid the necessity of requiring five T_1 lifetimes between successive RF excitations. Operating in a longitudinal steady state becomes a problem, however, when using spin echo trains in conjunction with low flip angle excitations, because imperfect 180° pulses will scramble the y and z components of magnetization, leading to mixing of different components of magnetization (*30*). Choi *et al.* (*15*) have suggested a solution to this problem, using the XY-16 (or XY-8 depending on the required length of echo train) sequence proposed by Guillion and colleagues (*31, 32*; see also *30, 33*). The XY-16 phase cycling sequence preserves all three components of magnetization, thereby preventing mixing of the transverse magnetization with the longitudinal steady state. The T_1 recovery period, TR, is then the time between the end of the echo train and the following excitation pulse. The signal equation, in the longitudinal steady state, is therefore given as (*13*)

$$S(\vec{k}) = \rho \cdot \exp\left[-\frac{TE(\vec{k})}{T_2}\right]$$
$$\times \left(\frac{1 - \exp(-TR/T_1)}{1 - \cos\theta \cdot \exp(-TR/T_1)} \sin\theta\right), \quad [1]$$

where θ is the RF flip angle, and ρ is the nuclear spin density. The dependence of TE on the k-space coordinate is discussed below. We note that while the act of acquiring data in the steady state will decrease S/N, the inherently large S/N per scan generally allows us to sacrifice S/N for the sake of imaging speed.

The use of XY-16 does, however, necessitate the use of two signal averages, not for S/N reasons, but rather because the XY-16 sequence acquires echoes which are phased on two different axes, leading to (on our system) two different baseline offsets in the data. This therefore requires a two-step phase cycle to obtain baseline correction, rather than a simple baseline correction during data processing. Future developments should allow us to acquire images without the need for phase cycling.

EXPERIMENTAL

Sample Description and Image Acquisition Parameters

Uniform test phantoms were 8-mm^3 CuSO$_4$ doped agarose gels (Sigma Chemical) contained in plastic UV-visible cuvettes. The T_2 relaxation parameters of the four phantoms used were 5, 10, 25, and 50 ms.

Two-dimensional images (64 × 64) of the four phantoms were acquired with a field-of-view (FOV) of 3.8 × 3.8 cm, using a phase encode time, t_p, of 400 μs, an interecho time of TE = 1.3 ms, and 90° excitation pulses, in a total imaging time of 4 min. The repetition time was chosen to be five times the longest spin–lattice relaxation time, T_{1L} (TR/T_{1L} = 5). A two-dimensional image (64 × 64) of the short T_2 gel alone was acquired in 2 min using an interecho time of TE = 1.2 ms, a TR of 120 ms, and a phase encode time of 400 μs.

A water-saturated sand was prepared using quartz sand (Atlantic Silica, Sussex, Canada) which was sieved so as to contain particles in a size range of 500 to 710 μm. The water-saturated sand was not prewashed or treated in any manner. Some paramagnetic impurities are likely present on the surface of the particles. The sample was contained in a plastic UV-visible cuvette. Due to the large intergrain space of the material, the T_1 and T_2 of the saturated sand were quite long ($\approx$1 s and 300 ms, respectively), while the effective T_2^* was more than two orders of magnitude shorter ($T_2^* \approx 800 \ \mu$s) after shimming.

A three-dimensional image (128 × 128 × 64) of the water-saturated sand was obtained in 8 h with a FOV of 19.2 ×

19.2 × 14.1 mm, using two signal averages acquired with an audio filter bandwidth of 3000 Hz. Data were acquired in a steady state (TR/T_1 = 0.2) using Ernst angle excitations (α = 30°), with an interecho time of 2 ms and a phase encode time of 400 μs.

A highly vesicular (volcanic) aggregate, Tepexil, of Mexican origin, was used as an example of a naturally occurring porous medium. This particular aggregate was chosen for its low iron content. Measured relaxation times were multiexponential and varied with saturation level. The longest relaxation components were approximately 1 s for T_1 and 200 ms for T_2 (measured with an echo time of TE = 200 μs). The linewidth was also saturation level dependent and was approximately 2500 Hz ($T_2^* \approx 150$ μs). Aggregates were hydrated by being soaked in distilled water for 1 month. The vial containing the aggregate was periodically rotated so as to allow air bubbles on the bottom of the sample to surface. Initially the rock had a specific gravity less than water; however, after approximately 1 week of water absorption, the specific gravity became greater than one.

An image of the saturated aggregate was acquired in three dimensions (64 × 64 × 32) in a total imaging time of 2 h, with a FOV of 3.8 × 3.8 × 3.8 cm. The data were obtained in a longitudinal steady state (TR/T_1 = 0.2) using Ernst angle excitations (α = 30°), with an interecho time of 0.9 ms and a phase encode time of 200 μs.

The saturated aggregate was then placed in a hydrated mortar. The sample holder was first partially filled with plastic mortar, and the aggregate was placed on top. The container was then filled and vibrated for 3 s. The mortar (w/c = 0.5) was prepared with white Portland cement (Lehigh Cement, PA) and fine quartz aggregates (Atlantic Silica, Sussex, Canada) and was cured in a moist curing room at 21°C and 100% relative humidity for 1 week. Relaxation times of water in the hydrated cement matrix are approximately 1 ms for T_1 and 0.5 ms for T_2, with a linewidth of roughly 2500 Hz ($T_2^* \approx 150$ μs).

The three-dimensional turboSPI image (64 × 64 × 64) of the hardened aggregate/mortar system was acquired in a steady state (TR/T_1 = 0.2) with a FOV of 4.7 × 4.7 × 5.8 cm in 4 h, with an interecho time of 0.9 ms, an encoding time of 200 μs, Ernst angle excitations (α = 30°), and an audio filter bandwidth of 7000 Hz. The three-dimensional SPRITE (*19, 20*) image (64 × 64 × 64) of the same sample was obtained using an RF flip angle of 45°, an interpulse time of 2.2 ms, and a phase encoding time of 110 μs. The resulting image had a FOV of 4 × 4 × 5.2 cm and was obtained in 1 h using two signal averages.

Imaging Hardware

All experiments were implemented on a TecMag (Houston, TX) Libra S-16 console, using a Nalorac (Martinez, CA) 2.35-T 32-cm-id horizontal bore superconducting magnet. A water-cooled 7.5-cm-id Nalorac gradient set (maximum gradi-
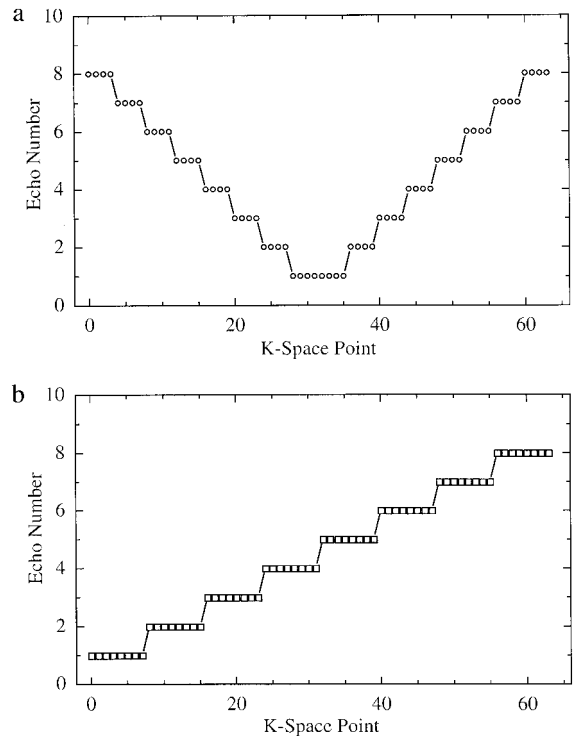

FIG. 2. Two possible turboSPI 64-point *k*-space trajectories for an echo train length of 8. (a) "centric ordering": Early echoes are acquired at the *k*-space center. Images acquired with this trajectory exhibit low contrast and high sensitivity. (b) "linear ordering": Echoes are acquired in a linear order from one extreme of *k*-space to the other, with the middle echoes acquired at the center of *k*-space. In this case the 4th and 5th echoes are acquired at the center, leading to an effective echo time of approximately TE$_{eff}$ = 5*TE. Images acquired with this trajectory exhibit increased contrast and decreased sensitivity.

ent 100 G/cm), driven by Techron (Elkhart, IN) 8710 amplifiers, was employed. All measurements were performed at ambient temperature and humidity, using an eight-rung birdcage coil (Morris Instruments, Ottawa) driven in quadrature by a 2-kW AMT (Brea, CA) 3445 RF amplifier.

RESULTS: EVALUATION OF PULSE SEQUENCE

Image Contrast in turboSPI

As with the standard RARE sequence, the number and order of *k*-space points acquired influence the acquisition speed, T_2 weighting, and sensitivity. We typically acquire ETLs of 8 to 16 echoes, obtained nonsequentially and then reordered and interleaved during image processing. The *k*-space data obtained using multiple echos are modulated by both relaxation and sequence timing parameters and therefore "filtered" in reciprocal space (*26, 34–37*). Many different *k*-space trajectories are possible, such as those shown in Fig. 2. This paper will focus on segmentation of *k*-space in one dimension only; however, we note that *k*-space may be segmented in many other ways, such as along spiral trajectories.
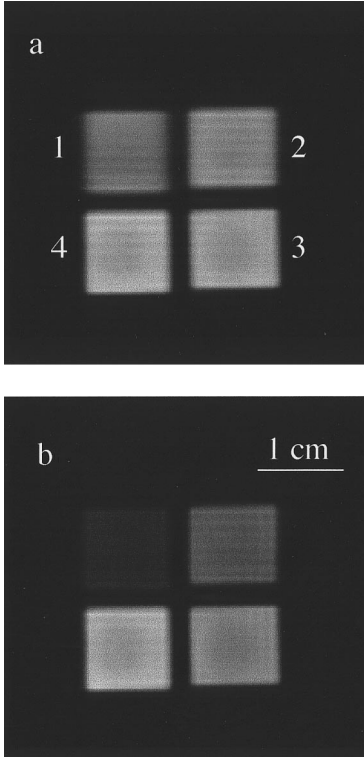
FIG. 3. Two-dimensional turboSPI images of four $CuSO_4$ doped agarose gels with T_2's of 5, 10, 25, and 50 ms for gels 1, 2, 3, and 4, respectively. (a) Data acquired using centric phase encode ordering (TE_{eff} = TE = 1.3 ms). Blurring of the image in the turboSPI (horizontal) direction is caused by T_2 modulation of the k-space data and is more severe for shorter T_2 samples. (b) An image with all parameters as in (a), but acquired using linear phase encode ordering (TE_{eff} = 5*TE = 6.5 ms). Note the increase in spin–spin relaxation contrast. Due to the different k-space trajectory, the image exhibits decreased blurring, but now has slightly increased edge ringing for shorter T_2 samples.

It can be demonstrated through Eq. [2] (*13*) that

$$S(\vec{\mathbf{k}}) = \int \int \rho(\vec{\mathbf{r}}) R(\vec{\mathbf{r}}) \exp[i 2\pi \vec{\mathbf{k}} \cdot \vec{\mathbf{r}}] d\vec{\mathbf{r}}, \qquad [2]$$

where $\rho(\mathbf{r})$ is the nuclear spin density and $R(\mathbf{r})$ is a term describing the relaxation times as a function of space, that while data at the k-space extremes ("high-frequency" data) determine edge resolution, image contrast is determined by the weighting of the signal obtained at the k-space center ("low-frequency" data). This is often exploited in fast spin echo (FSE) imaging and is the origin of the relaxation enhancement feature of RARE imaging (*26, 27*). Of particular importance here is the ability to introduce and manipulate the spin–spin relaxation image contrast though the choice of k-space trajectory, while keeping the actual interecho time short to minimize diffusion-based signal loss.

Figure 3 demonstrates the image contrast obtained when imaging four agarose gels, doped with $CuSO_4$ so as to have varying T_2's. The image in Fig. 3a was obtained using the k-space trajectory shown in Fig. 2a, in which early echoes are collected at the k-space center ("centric ordering"). Images obtained in this manner have an effective echo time, TE_{eff}, which is simply equal to TE, and the resulting image is therefore ρ-weighted. When the image is obtained using the trajectory shown in Fig. 2b, however, where the central k-space data are collected using the fourth and fifth echoes ("linear ordering"), significant T_2 contrast is visible in the image, as shown in Fig. 3b. The effective echo time is therefore approximately 5*TE, while still maintaining an interecho time of only TE. The calculated image contrast (1.0:0.87:0.59:0.31) is in reasonable agreement with the measured relative image intensities (1.0:0.83:0.56:0.25). The images were acquired with different k-space trajectories, but otherwise identical image acquisition parameters.

The turboSPI Point Spread Function

Amplitude modulation of the k-space data, defined by the modulation transfer function (MTF), not only affects contrast, but also leads to a change in the measured point-spread function (PSF), following Fourier transformation. For our purposes, the total MTF can be considered to be due to three terms, $MTF_{k\text{-space}}$, the MTF due to the size of k-space sampled, $MTF_{diffusion}$, the MTF due to molecular diffusion, and MTF_{turbo}, the MTF due to weighting introduced by the imaging sequence itself, as shown in Eqs. [3] and [4] (*13, 39*):

$$MTF = MTF_{k\text{-space}} \times MTF_{diffusion} \times MTF_{turbo} \qquad [3]$$

$$\Updownarrow FFT$$

$$PSF = PSF_{k\text{-space}} \otimes PSF_{diffusion} \otimes PSF_{turbo}. \qquad [4]$$

Loss of resolution takes place when the full width at half height of the resulting PSF is larger than the pixel size. Ideally, we would like the limiting factor on resolution to be simply due to the size of our sampled k-space. This requires minimizing or, when possible, removing the MTF due to both diffusion and the imaging method. In the first instance, the turboSPI technique acts to minimize the MTF due to diffusion through the use of short gradient pulses and interecho times. The term of interest then becomes the MTF due to the turboSPI imaging parameters and k-space trajectory. The effect of the MTF_{turbo} is to increase the width of the PSF and, in addition, the discontinuities in the MTF lead to a slight ringing (*34, 35, 38, 39*) in the turboSPI imaging direction.

These features are also observed in the images shown in Fig. 3, where we see that when using centric order encoding (Fig. 3a) short T_2 samples exhibited increased blurring in the direction of the turboSPI modulation, while short T_2 samples exhibited increased edge ringing using linear order encoding (Fig. 3b).

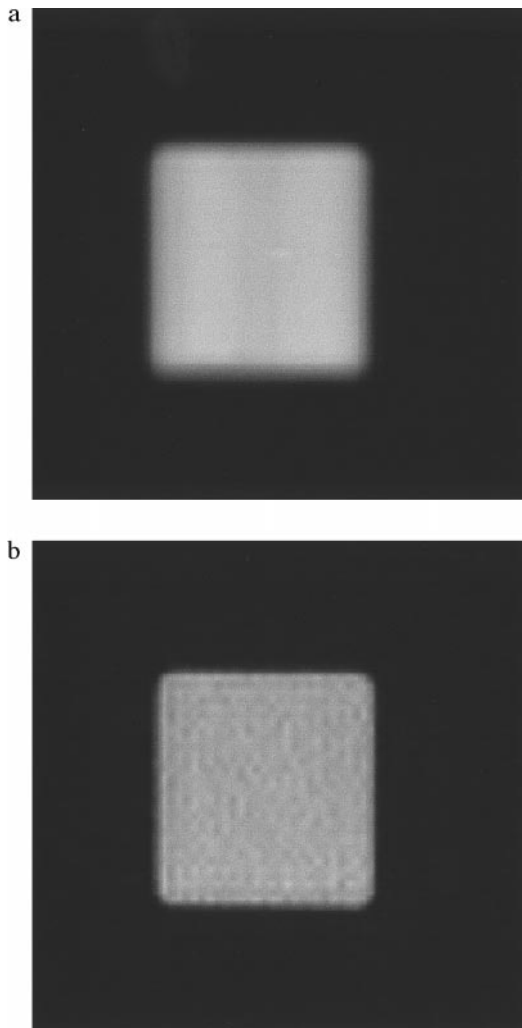A proper choice of k-space trajectory, ETL, and echo time

FIG. 4. (a) A 2D turboSPI image of a $CuSO_4$ doped agarose gel with a T_2 of approximately 5 ms. The data were acquired using centric phase encode ordering ($TE_{eff} = TE = 1.2$ ms). Image blurring in the turboSPI (horizontal) direction is caused by the T_2 modulation of the k-space trajectory. (b) The same turboSPI image as in (a), with deconvolution performed during image processing to remove the modulation effects of the imaging sequence. Note the increase in edge resolution (and decrease in S/N).

quiring a sample echo train with all phase encoding gradients off), we can obtain the MTF_{turbo} shown in Fig. 6a and thereby deconvolve the image. The deconvolution acts to correct all modulations in the resulting data (*40*) whether they are due to spin echo decay or the creation of stimulated echoes. Echo trains acquired with and without the phase encode gradient are equivalent because the net gradient area in the RARE imaging method is zero regardless of the phase encode gradient amplitude. The resulting deconvolution of the PSF_{turbo} removes the ghosting and ringing artifacts and decreases the FWHM of the total PSF, as shown in Fig. 6b. The deconvolved image and corresponding 1D profile are shown in Figs. 4b and 5b, respectively, exhibiting decreased edge blurring (with a S/N penalty). We note that acquisition of the MTF adds a time of only several hundreds of milliseconds to the overall imaging length, and the resulting deconvolution does not alter the desired image contrast; however, this method will work optimally only for samples with a spatially homogeneous T_2.

Active Spoiling in turboSPI

It is well known that the consequence of using fast multi-pulse sequences is the creation of unwanted coherences (*41–44*). These coherences can be created by the repetition of excitation pulses with times on the order of or shorter than T_2, as in FLASH imaging (*45–51*), or due to repeated imperfect refocusing pulses in FSE sequences (*52–55*). The creation of

will often lead to a PSF which is resolution-limited purely by the k-space sampling window. Correct use of the sequence requires balancing the desired relaxation weighting with image acquisition time and resolution.

Method of turboSPI Deconvolution

In some cases, however, such as in high-resolution imaging, the resolution may be limited by the PSF due to the echo train. The image shown in Fig. 4a of a $CuSO_4$ doped gel with a T_2 of approximately 5 ms was acquired using centric encoding, with image acquisition parameters chosen so as to exhibit severe blurring in the turboSPI direction. By then acquiring an echo train amplitude/phase "template," however (obtained by ac-
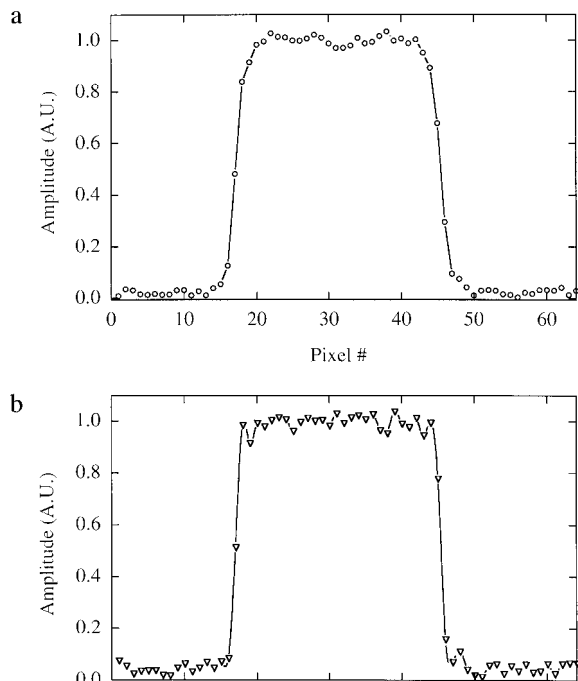

FIG. 5. One-dimensional slices through the (a) raw image and (b) deconvolved image of the $CuSO_4$ doped agarose gel ($T_2 \approx 5$ ms) shown in Fig. 4, demonstrating both the increase in edge resolution and the decrease in S/N following deconvolution.
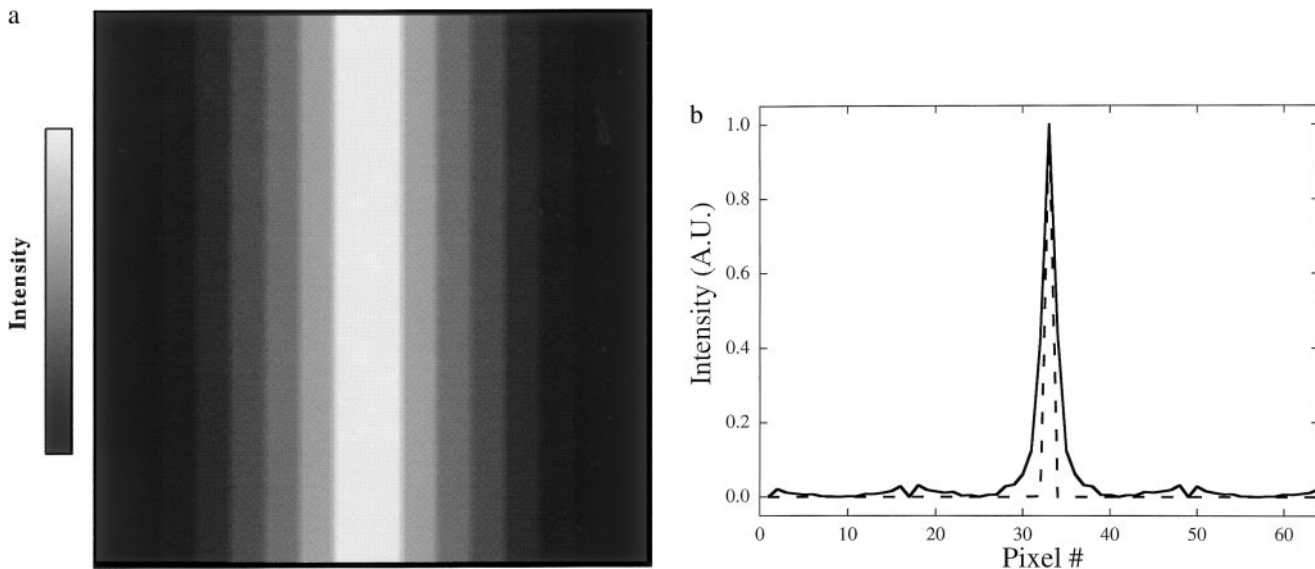
FIG. 6. (a) A 2D modulation transfer function (MTF) for a turboSPI image of a $CuSO_4$ doped agarose gel with a T_2 of approximately 5 ms. The data were acquired using centric phase encode ordering ($TE_{eff} = TE = 1.2$ ms). (b) The point spread function (PSF) obtained from Fourier transformation of the above MTF, shown before (solid line) and after (dotted line) deconvolution. Note the decrease in width of the central peak of the PSF, as well as the absence of ringing (caused by the discontinuities in the MTF) in the PSF following deconvolution.

unwanted spin and stimulated echoes can therefore be especially large when using turboSPI in the steady state, as it utilizes a combination of FLASH-like low flip angle excitations with short repetition times and RARE-like echo trains.

This problem is typically avoided in FLASH imaging through the application of spoiling gradients during the time TR. The avoidance of unwanted echoes in FSE techniques has been previously discussed by Hennig and colleagues (*26, 27, 41, 42*). The use of the RARE-type gradient scheme, in which net gradient area between refocusing pulses is zero, avoids image artifacts caused by the encoding of stimulated echoes. This does, however, lead to contrast which is a mixture of T_1 and T_2, as has been discussed by Crawley and Henkelman (*55*). In steady-state turboSPI this is not a concern, however, as the contrast will already be dependent on both T_1 and T_2. When pure T_2 contrast is desired, the spoiling scheme based on that of Crawley and Henkelman has been shown to time shift the stimulated echoes away from the echo center.

RESULTS: turboSPI IMAGING OF POROUS MATERIALS

Saturated Quartz Sand

As an intermediate step between a overly simple "model" porous medium, such as glass beads, and a natural rock, we first demonstrate the use of turboSPI in imaging a water-saturated quartz sand. Aggregates of this type are quite impermeable and do not significantly absorb water, and all observable water therefore exists in the pore space between sand grains.

The long T_2 of the sample allows us to obtain many echoes

in a single echo train without a large decrease in echo amplitude. Since in this case we wish to acquire the image with reasonably fine resolution, however, we trade off imaging speed with k-space modulation and acquire the image with an ETL of 16 (using centric k-space acquisition order). A 2D slice from the 3D data set is shown in Fig. 7, with in-plane resolution of 150×150 μm and a slice thickness of 220 μm. This high-resolution image has excellent S/N and exhibits no ob-
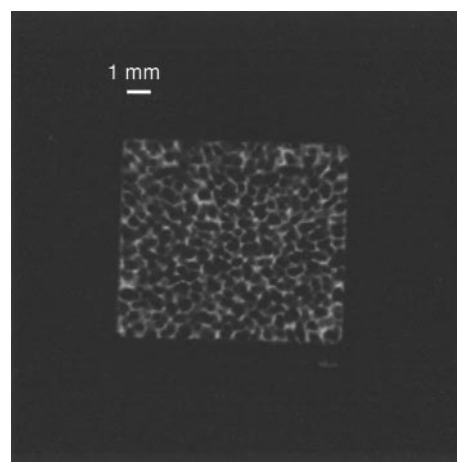

FIG. 7. A 2D slice from a 3D turboSPI image of a water-saturated quartz sand ($T_1 = 1$ s, $T_2 = 300$ ms, $T_2^* = 800$ μs). In-plane resolution is 150×150 μm, with a slice thickness of 220 μm. The sand grains are 500–710 μm and were not prewashed. The quartz has very low absorption, and therefore all water is contained within the intergrain space. A small amount of masking tape is visible in the bottom right of the image.

servable image artifacts due to susceptibility nor any significant resolution loss due to the *k*-space modulation.

This image may be compared to the images obtained by Manz *et al.* (*7*) using π-EPI. While turboSPI will never compete in terms of temporal resolution, EPI imaging of idealized model materials neglects T_2^* effects which may degrade image quality, because of the difficulty in rapidly switching gradients large enough to overcome local susceptibility-induced gradients (*11*).

Partially Saturated Tepexil Rock

The technique was then applied to a naturally occurring rock, Tepexil, of Mexican origin. Initial NMR relaxation studies of these aggregates indicated that T_2 is strongly dependent on echo time. This result is not surprising considering the heterogeneity of the material, which is further reflected in the fact that T_2^* is three orders of magnitude shorter than T_2. This demonstrates the necessity of using an imaging technique with short interecho times in order to minimize diffusional losses.

Two-dimensional images from a three-dimensional data set of a partially saturated Tepexil aggregate, which were acquired using an ETL of 8 and centric encoding, are shown in Fig. 8. The images reveal an inhomogeneous distribution of water within the aggregate, with the most noticeable feature being the presence of large voids. Further study is necessary to determine whether these voids are true voids or if this is a relaxation effect. To determine this the voids will be further studied by both MRI and electron microscopy. Traditional (non-MRI) studies of similar aggregates (*56*) have shown the presence of conduits and indicate that most absorption occurs in the first 5 min via capillary suction, and the rate of further absorption is determined by a much slower diffusion process which continues for approximately 1 year (*57*).

Tepexil Aggregates in a Hydrated Cement Matrix

One particular application of this work is the study of porous aggregates in a hydrated cement matrix (so-called "lightweight concrete" (*58*)). An optical picture of a simple lightweight concrete, viewed in cross-section, is shown in Fig. 9. Lightweight concrete is a multi-billion-dollar industry and is used in civil structures throughout the world; however, there is currently no method, nondestructive or otherwise, to directly study the process of three-dimensional moisture migration in lightweight aggregates. It is well known that highly porous aggregates can either remove or add moisture to the interfacial matrix layer at the paste aggregate interface (*57, 58*), which can then greatly influence the bulk material properties and durability (*58*). The exact mechanism by which this takes place is a function not only of moisture movement within the aggregate itself, but also of moisture migration between the aggregate and the pore structure of the cement and the initial mixture conditions of both the fresh cement and the aggregates. As the local moisture content decreases at the interfacial layer
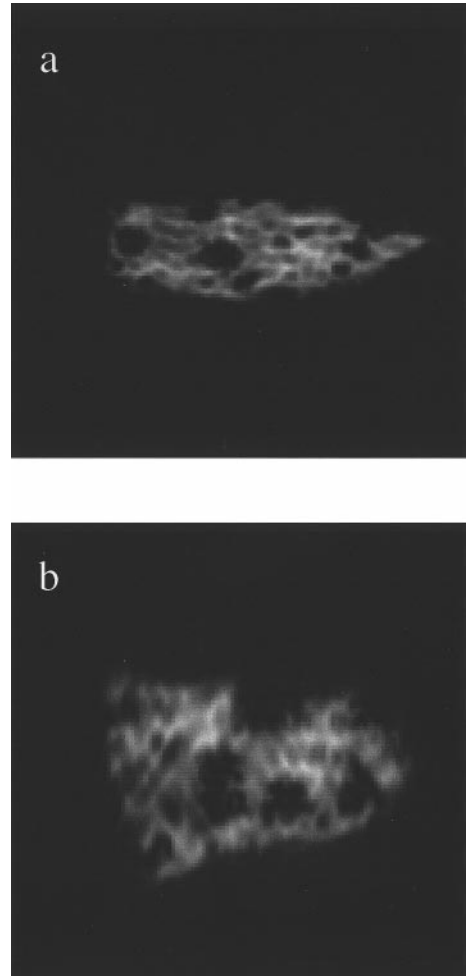

FIG. 8. Two 2D slices from a 3D turboSPI image of a water-saturated "Tepexil" aggregate ($T_{1L} \approx 1$ s, $T_{2L} \approx 200$ ms, $T_2^* = 0.15$ ms). Nominal voxel resolution is $0.6 \times 0.6 \times 1.2$ mm. Tepexil is a porous aggregate which is volcanic in origin. The aggregate was soaked in water for several weeks before imaging. The 3D image ($64 \times 64 \times 32$) was acquired in a steady state (TR/$T_1 = 0.2$) using Ernst angle excitations and centric phase encode ordering, with two signal averages and an audio filter bandwidth of 7000 Hz.

(whether due to sample drying or the hydration reaction) moisture may be removed from the aggregate so as to continue the chemical hydration of the cement. The ability to nondestructively determine local moisture content as a function of time would be a valuable tool in studying lightweight concrete.

MRI studies of moisture distribution in concrete have been demonstrated previously (*59–65*), using a T_2^*-weighted imaging technique called SPRITE (*19, 20*). SPRITE images of lightweight concrete show the porous aggregates as a void, as exhibited in Fig. 10, due to the fact that the fluid content (and corresponding NMR signal) is significantly lower in the aggregate compared to the surrounding paste. The aggregate is the same aggregate shown in the images of Fig. 8. Weighting the image by T_2^* is not possible, as the T_2^* value for the aggregate and cement paste is approximately the same, and
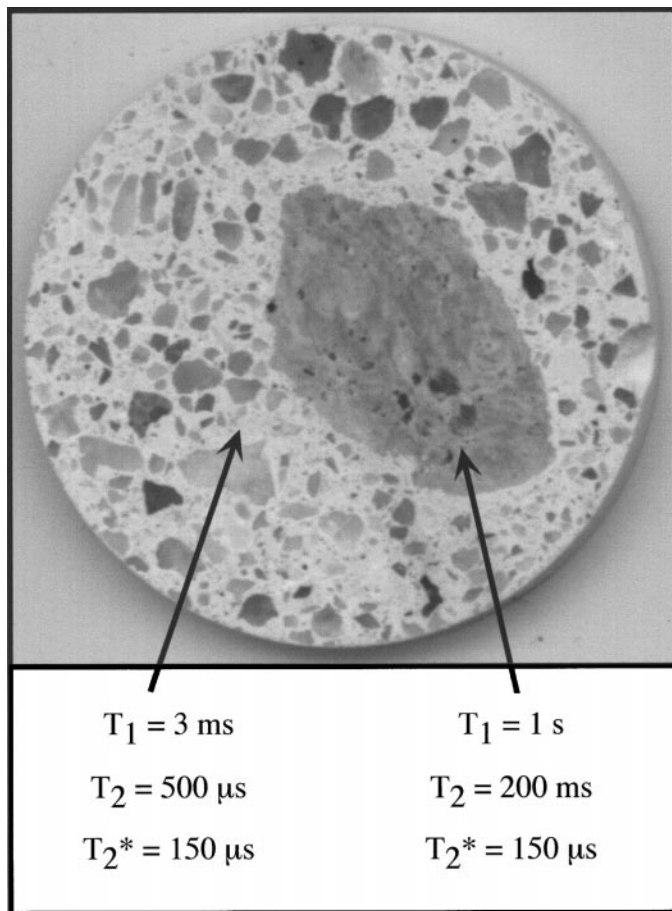
paste to decay (acquisition of this strong signal at the extreme of k-space leads to severe ringing artifacts).

These images demonstrate the ability of turboSPI to acquire a T_2-weighted image of the aggregate–mortar system, which allows for visualization of water within the aggregate. The images show a very different distribution of moisture in the aggregate when it is placed in a hardened mortar. While moisture is still present in the interior of the aggregate, a ring of high signal intensity is visible at the outer edge. Initial results indicate that this may be due to an influx of cement products during the initial setting stage (first 6 h) of the concrete, which has a very high local water to cement ratio.

We note that the ability to obtain images with no signal intensity from the surrounding mortar will allow us to "zoom" the image to increase the resolution of the region of interest.

CONCLUSIONS

The turboSPI technique has been shown to provide excellent S/N high-resolution images of highly heterogeneous materials with long T_2 but short T_2^*, using pure phase encoding with reasonable imaging times. The images exhibit no distortions or artifacts caused by susceptibility, shimming, chemical shift, stimulated echoes, and imperfect B_1. The technique allows the introduction of spin spin relaxation weighting with long effective echo times through the use interleaved k-space trajectories. In addition, we demonstrate the use of a method to deconvolve the effect of k-space modulation when necessary. We believe
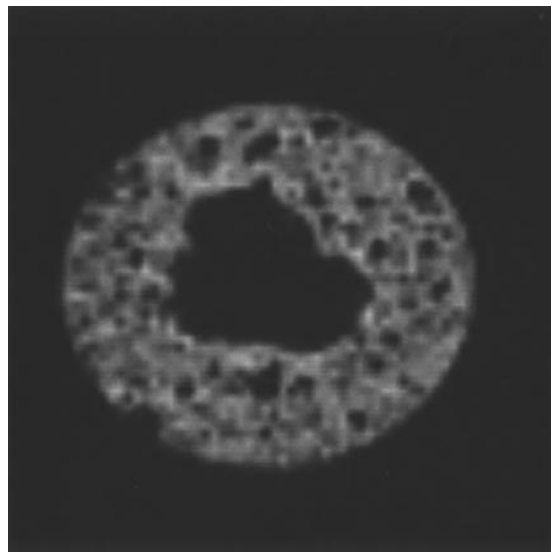

FIG. 9. An optical image of a single lightweight Tepexil aggregate contained in a hardened mortar (the same sample used in Figs. 8, 10, and 11). The image (shown of a sample which was physically cross-sectioned) was obtained using an Epson ES 1000C Desktop scanner. The inhomogeneous linewidths of the signal from water in the mortar and the aggregate are the same ($\approx$2500 Hz); however, the spin–spin and spin–lattice relaxation times in the mortar ($T_2 \approx 0.5$ ms, $T_1 \approx 3$ ms) and the aggregate ($T_{2L} \approx 200$ ms, $T_{1L} \approx 1$ s) are different due to differences in pore size and structure.

weighting by T_1 is not possible as it is very difficult to either suppress or null the very short T_1 of the cement ($\approx$3 ms). The T_2 values, however, are quite different. The turboSPI method is therefore well suited to the problem because it provides T_2-weighted images for short T_2^* materials and because the high sensitivity of the method helps to overcome the inherently low fluid content.

Two-dimensional slices from a three-dimensional data set acquired using turboSPI are shown in Fig. 11. These images are of the same sample shown in Figs. 9 and 10. The image exhibits roughly the reverse contrast to the image acquired using SPRITE, with the aggregate appearing as a bright signal and the faint signal from the cement matrix in the background. The data were obtained using linear k-space ordering, in which only the middle 8 echoes of an XY-16 echo train were encoded ($TE_{eff} = 8.1$ ms). The first 4 echoes in the train were not acquired so as to allow the very strong short T_2 signal from the

FIG. 10. A 2D transverse slice from a 3D data set obtained using the T_2^*-weighted pure phase encoding imaging technique SPRITE of a single Tepexil aggregate in a hardened mortar. Note that the Tepexil appears as a signal void, due to the fact that the moisture content is much lower in the aggregate than in the surrounding paste. Smaller voids in the image are the dense quartz fine aggregates which do not contain water.
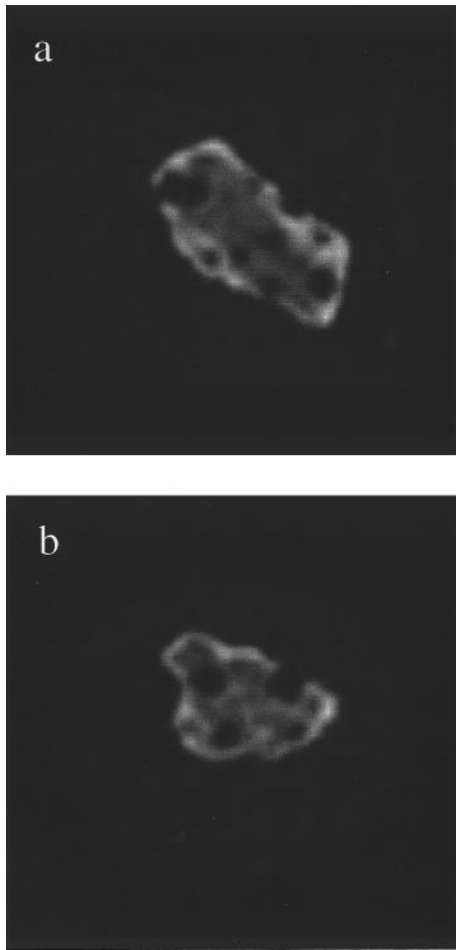
FIG. 11. (a) Longitudinal and (b) transverse 2D slices from a 3D data set obtained using turboSPI of a single Tepexil aggregate in a hardened mortar. The material is the same one shown in Fig. 10; however, the image has reverse contrast compared to the image acquired with SPRITE, due to the T_2-weighting of the image. Nominal voxel size is $740 \times 740 \times 910 \ \mu$m. The aggregate was soaked in water for several weeks before imaging. The 3D image ($64 \times 64 \times 64$) was acquired in a steady state (TR/$T_1 = 0.2$) using Ernst angle excitations in 4 h. The cement paste is faintly visible in the background of the image. While moisture is present in the interior of the aggregate, a ring of high signal intensity is visible at the outer edge. Initial results indicate that this may be due to an influx of cement products during the initial setting stage (first 6 h) of the concrete, which has a very high local water to cement ratio.

this technique will be a valuable tool in studying heterogeneous materials.

REFERENCES

1. A. T. Watson and C. T. Philip Chang, *Prog. NMR Spectrosc.* **31,** 343 (1997).

2. M. Peyron, G. K. Pierens, A. J. Lucas, L. D. Hall, G. F. Potter, R. C. Stewart, and D. W. Phelps, *Magn. Reson. Imaging* **12,** 295 (1994).

3. R. L. Kleinberg, *Magn. Reson. Imaging* **12,** 271 (1994).

4. W. P. Halperin, J-Y. Jehng, and Y-Q. Song, *Magn. Reson. Imaging* **12,** 169 (1994).

5. R. Blinc, J. Dolinsek, G. Lahajnar, A. Sepe, I. Zupancic, S. Zumer, F. Milia, and M. M. Pintar, *Z. Naturforsch.* **43a,** 1026 (1988).

6. P. McDonald and J. Strange, *Physics World,* 29 (1998).

7. B. Manz, P. S. Chow, and L. F. Gladden, *J. Magn. Reson.* **136,** 226 (1999).

8. S. Chen, X. Yao, J. Qiao, and T. Watson, *Magn. Reson. Imaging* **13,** 599 (1995).

9. S. N. Sarkar, E. W. Wooten, and R. A. Komoroski, *Appl. Spectrosc.* **45,** 619 (1991).

10. A. M. Peters, P. S. Robyr, R. W. Bowtell, and P. Mansfield, *Magn. Reson. Imaging* **14,** 875 (1996).

11. A. M. Peters and R. Bowtell, *J. Magn. Reson.* **137,** 196 (1999).

12. P. T. Callaghan, *J. Magn. Reson.* **87,** 304 (1990).

13. P. T. Callaghan, "Principles of Nuclear Magnetic Resonance Microscopy," Clarendon, Oxford (1991).

14. P. T. Callaghan, L. C. Forde, and C. J. Rofe, *J. Magn. Reson.* **104,** 34 (1994).

15. S. C. Choi, X-W. Tang and D. G. Cory, *Int. J. Imaging Syst. Technol.* **8,** 263 (1997).

16. S. Emid and J. H. N. Creyghton, *Physica* **128B,** 81 (1985).

17. S. Gravina and D. G. Cory, *J. Magn. Reson.* **104,** 53 (1994).

18. D. E. Axelson, A. Kantzas, and T. Eads, *Can. J. Appl. Spectrosc.* **40,** 16 (1995).

19. B. J. Balcom, R. P. MacGregor, S. D. Beyea, D. P. Green, R. L. Armstrong, and T. W. Bremner, *J. Magn. Reson. A* **123,** 131 (1996).

20. B. J. Balcom, SPRITE Imaging of Short Relaxation Time Nuclei, *in* "Spatially Resolved Magnetic Resonance: Methods, Materials, Medicine, Biology, Rheology, Geology, Ecology, Hardware" (P. Blumler, B. Blumich, R. Botto, and E. Fukushima, Eds.), Wiley–VCH, Weinham (1998).

21. R. Pohmann, M. von Kienlin, and A. Haase, *J. Magn. Reson.* **129,** 145 (1997).

22. W. A. Edelstein, J. M. S. Hutchinson, G. Johnson, and T.W. Redpath, *Phys. Med. Biol.* **25,** 751 (1980).

23. J. C. Sharp, R. W. Bowtell, and P. Mansfield, *Magn. Reson. Med.* **29,** 407 (1993).

24. J. B. Miller and A. N. Garroway, *J. Magn. Reson.* **67,** 575 (1986).

25. D. J. O. McIntyre, F. Hennel, and P. G. Morris, *J. Magn. Reson.* **130,** 58 (1998).

26. J. Hennig, A. Nauerth, and H. Friedburg, *Magn. Reson. Med.* **3,** 823 (1986).

27. J. Hennig, *J. Magn. Reson.* **78,** 397 (1988).

28. A. Haase, J. Frahm, D. Matthaei, W. Haenicke, and K.-D. Merboldt, *J. Magn. Reson.* **67,** 258 (1986).

29. A. Haase, *Magn. Reson. Med.* **13,** 77 (1990).

30. A. A. Maudsley, *J. Magn. Reson.* **69,** 488 (1986).

31. T. Gullion, D. B. Baker, and M. S. Conradi, *J. Magn. Reson.* **89,** 479 (1990).

32. T. Gullion, *J. Magn. Reson. A* **101,** 320 (1993).

33. T. J. Norwood and S. C. R. Williams, *J. Magn. Reson.* **94,** 419 (1991).

34. R. V. Mulkern, S. T. S. Wong, C. Winalski, and F. A. Jolesz, *Magn. Reson. Imaging* **8,** 557 (1990).

35. R. V. Mulkern, P. S. Melki, P. Jakab, N. Higuchi, and F. A. Jolesz, *Med. Phys.* **18,** 1032 (1991).

36. R. T. Constable, R. C. Smith, and J. C. Gore, *J. Comput. Assist. Tomogr.* **16,** 41 (1992).

37. P. Jhooti, F. Weismann, A. M. Taylor, P. D. Gatehouse, G. Z. Yang, J. Keegan, D. J. Pennell, and D. N. Firmin, *J. Magn. Reson. Imaging* **8,** 968 (1998).

38. X. Zhou, Z. Liang, G. P. Cofer, C. F. Beaulieu, S. A. Suddarth, and G. A. Johnson, *J. Magn. Reson. Imaging* **3,** 803 (1993).

39. C. F. M. Williams and T. W. Redpath, *Magn. Reson. Med.* **41,** 63 (1999).

40. J. Coremans, M. Spanoghe, L. Budinsky, J. Sterckx, R. Luypaert, H. Eisendrath, and M. Osteaux, *J. Magn. Reson.* **124,** 323 (1997).

41. J. Hennig, *Concepts Magn. Reson.* **3,** 125 (1991).

42. J. Hennig, *Concepts Magn. Reson.* **3,** 179 (1991).

43. D. Burstein, *Concepts Magn. Reson.* **8,** 269 (1996).

44. P. B. Kingsley, *Concepts Magn. Reson.* **7,** 115 (1995).

45. C. F. M. Williams, T. W. Redpath, and F. W. Smith, *Magn. Reson. Imaging* **14,** 419 (1996).

46. J. H. Duyn, *Magn. Reson. Med.* **37,** 559 (1997).

47. J. Frahm, W. Hanicke, and K-D. Merboldt, *J. Magn. Reson.* **72,** 307 (1987).

48. Y. Zur, M. L. Wood, and L. J. Neuringer, *Magn. Reson. Med.* **21,** 251 (1991).

49. A. P. Crawley, M. L. Wood, and R. M. Henkelman, *Magn. Reson. Med.* **8,** 248 (1988).

50. R. B. Buxton, C. R. Fisel, D. Chien, and T. J. Brady, *J. Magn. Reson.* **83,** 576 (1989).

51. H. Z. Wang and S. J. Reiderer, *Magn. Reson. Med.* **15,** 175 (1990).

52. X. Wan, D. L. Parker, J. N. Lee, H. R. Buswell, and G. T. Gullberg, *Magn. Reson. Med.* **34,** 632 (1995).

53. R. S. Hinks and R. T. Constable, *Magn. Reson. Med.* **32,** 698 (1994).

54. S. Majumdar, S. C. Orphanoudakis, A. Gmitro, M. O'Donnell, and J. C. Gore, *Magn. Reson. Med.* **3,** 397 (1986).

55. A. P. Crawley and R. M. Henkelman, *Magn. Reson. Med.* **4,** 34 (1987).

56. T. W. Bremner, Ph.D. Thesis, Imperial College, University of London, London (1981).

57. O. S. Ooi, M.Sc. Thesis, University of New Brunswick, Fredericton, New Brunswick, Canada (1985).

58. P. K. Mehta, "Concrete Structure, Properties and Materials," Prentice Hall, Englewood Cliffs, NJ (1986).

59. P. J. Prado, B. J. Balcom, S. D. Beyea, R. L. Armstrong, and T. W. Bremner, *Solid State NMR* **10,** 1 (1997).

60. S. D. Beyea, B. J. Balcom, T. W. Bremner, P. J. Prado, D. P. Green, R. L. Armstrong, and P. E. Grattan-Bellew, *Cem. Conc. Res.* **28,** 453 (1998).

61. P. J. Prado, B. J. Balcom, S. D. Beyea, R. L. Armstrong, T. W. Bremner, and P. E. Grattan-Bellew, *Mag. Reson. Imaging* **16,** 521 (1998).

62. P. J. Prado, B. J. Balcom, S. D. Beyea, T. W. Bremner, R. L. Armstrong, Rashmi Pishe, and P. E. Grattan-Bellew, *J. Phys. D Appl. Phys.* **31,** 2040 (1998).

63. S. D. Beyea, B. J. Balcom, P. J. Prado, A. R. Cross, C. B. Kennedy, R. L. Armstrong, and T. W. Bremner, *J. Magn. Reson.* **135,** 156 (1998).

64. P. J. Prado, B. J. Balcom, S. D. Beyea, T. W. Bremner, R. L. Armstrong, and P. E. Grattan-Bellew, *Cem. Conc. Res.* **28,** 261 (1998).

65. S. D. Beyea, B. J. Balcom, T. W. Bremner, P. J. Prado, A. R. Cross, R. L. Armstrong, and P. E. Grattan-Bellew, *Solid State NMR,* **13,** 93 (1998).